PHYSICAL REVIEW B **91**, 045132 (2015)

Prediction of phonon-mediated high-temperature superconductivity in $Li_3B_4C_2$

Miao Gao,[1,2] Zhong-Yi Lu,[2,*] and Tao Xiang[1,3,†]
[1]*Institute of Physics, Chinese Academy of Sciences, Beijing 100190, China*
[2]*Department of Physics, Renmin University of China, Beijing 100872, China*
[3]*Collaborative Innovation Center of Quantum Matter, Beijing, China*

(Received 20 June 2014; revised manuscript received 31 December 2014; published 21 January 2015)

Based on the first-principles density functional theory calculations for the electronic band structure and lattice dynamics of $Li_3B_4C_2$, we predict that this material is a strong electron-phonon coupled superconductor with a superconducting transition temperature higher than that for MgB_2. $Li_3B_4C_2$ is a layered material which is formed by substituting one-third carbon atoms in the semiconducting compound LiBC with boron atoms, with the remaining carbon atoms forming a regular hexagonal lattice in each boron-carbon layer. Similar to MgB_2, $Li_3B_4C_2$ is inherently metallic and possesses two σ-bonding bands around the Fermi energy. The superconductivity in this material arises from the coupling of these two σ-bonding bands with the intralayer bond-stretching E' modes. From the phonon spectrum and the formation energy, we find that $Li_3B_4C_2$ is dynamically stable and has a high probability to be synthesized in laboratory.

DOI: 10.1103/PhysRevB.91.045132 PACS number(s): 74.25.Kc, 63.20.kd, 74.20.Pq, 74.70.Dd

I. INTRODUCTION

A σ bond in graphite or other materials is a strong covalent bond of a spin singlet pair formed by two electrons with opposite spins. In most materials, a σ bond is a stable bound state whose energy sinks well below the Fermi level, making no contribution to conductivity. However, if the energy of a σ bond is lifted up to the Fermi level by hole doping or other effects, the binding force of the bond is released and electrons become itinerant. The characteristic feature of the σ bond can nevertheless be retained if its hybridization with other conducting electrons is small. Since the coupling between σ-bonding electrons and lattice vibrations is generally very large, this may generate a strong attractive interaction to pair electrons into a high-T_c superconducting state.

This is just the physics underlying the 39 K superconductivity in MgB_2, discovered by Akimitsu and co-workers in 2001 [1]. This picture was supported by the density functional theory and lattice dynamics calculations, which show that the electron-phonon coupling (EPC) between the σ-bonding bands and the bond-stretching optical E_{2g} phonon modes [2–6] plays a central role in the superconducting pairing in MgB_2, and was further confirmed by isotope effect measurements [7]. Stimulated by the discovery of superconductivity in MgB_2, great efforts have been made in recent decades to find new phonon-mediated superconductors among sp^3- or sp^2-hybridized σ-bonding compounds by lifting the σ-bonding bands up to the Fermi level through hole doping or other effects [8].

Superconductivity in sp^3-hybridized σ-bonding compounds was first discovered at about 4 K in diamond with 2.8% boron substitution [9], and then at 11 K in thin diamond films with 5% boron substitution [10]. If the boron concentration is further increased to 20%–30%, it was predicted from first-principles density functional calculations that diamond may become superconducting at about 55 K [11]. However, such high doping concentrations have never been achieved experimentally [12].

For sp^2-hybridized σ-bonding compounds, the EPC studies focus more on calcium intercalated graphite, CaC_6, and lithium deficient Li_xBC. Superconductivity in CaC_6 was found at 11.4 K [13], and then raised up to 15.1 K under 8 GPa hydrostatic pressure [14]. But unlike in MgB_2, the strong covalent σ-bonding band lies well below the Fermi level and the superconducting pairing is caused by the EPC between electrons and soft phonon modes of calcium in this material [15,16]. LiBC is a large-gap semiconductor with a boron-carbon σ-bonding band at the top of the valence bands [17–19]. It was suggested that the σ-bonding band can be rigidly lifted up to the Fermi level by removing some lithium atoms, leading to a phonon-mediated superconductor with a T_c about 100 K [19]. However, superconductivity has never been observed in hole-doped Li_xBC [20–22]. The reason for this is that hole doping by creating Li deficiencies introduces strong lattice distortion in both Li and boron-carbon layers. This changes the band structure of LiBC entirely and suppress the effects lifting the σ-bonding band up to the Fermi level [23]. $Li_{0.5}BC$ remains in the semiconducting phase.

Doping holes in LiBC by partially substituting carbon atoms with boron atoms is experimentally more feasible. This will not introduce any lattice distortion. In this paper, we present a first-principles density functional theory study for two boron-substituted LiBC-type compounds, namely $Li_3B_4C_2$ and Li_2B_3C. On both materials, we find that partial substitution of carbon by boron atoms can lift the σ-bonding bands up to the Fermi level and lead to a strong EPC. Based on the EPC, the other parameters obtained, and the Allen-Dynes formula, we predict that these materials are strong phonon-mediated high-temperature superconductors, with T_c higher than that of MgB_2. From the formation energies (see Appendix B), we find that $Li_3B_4C_2$ is energetically more stable than Li_2B_3C. Thus in the main text, we will focus the discussion on $Li_3B_4C_2$. A detailed discussion of the band structure and lattice dynamics of Li_2B_3C is presented in Appendix A.

---

[*] zlu@ruc.edu.cn
[†] txiang@iphy.ac.cn

II. COMPUTATIONAL DETAILS

In our first-principles electronic structure calculations, the plane wave basis method is used [24]. We adopt the generalized gradient approximation (GGA) with Perdew-Burke-Ernzerhof formula [25] for the exchange-correlation potentials. The Rappe-Rabe-Kaxiras-Joannopoulos ultrasoft pseudopotentials [26] are used to model the electron-ion interactions. After the full convergence test, the kinetic energy cutoff and the charge density cutoff of the plane wave basis are chosen to be 40 Ry and 480 Ry, respectively. We use the Marzari-Vanderbilt smearing technique [27] of width 0.02 Ry with a $18 \times 18 \times 18$ **k**-point grid to evaluate the self-consistent electron density, and a $36 \times 36 \times 36$ **k**-point grid to determine the Fermi-surface contours. Phonon wave vectors are sampled on a $6 \times 6 \times 6$ mesh. The lattice constants after full relaxation are adopted.

The phonon properties and EPC are calculated based on density functional perturbation theory [28] and Eliashberg equations [29]. The electron-phonon interaction matrix element $g^{ij}_{\mathbf{k},\mathbf{q}\nu}$, which describes the probability amplitude for scattering of an electron with a transfer of crystal momentum $\mathbf{q}$, is determined by [30,31]

$$g^{ij}_{\mathbf{k},\mathbf{q}\nu} = \left(\frac{\hbar}{2M\omega_{\mathbf{q}\nu}}\right)^{1/2} \langle \psi_{i,\mathbf{k}} | \frac{dV_{\mathrm{SCF}}}{d\hat{u}_{\mathbf{q}\nu}} \cdot \hat{e}_{\mathbf{q}\nu} | \psi_{j,\mathbf{k}+\mathbf{q}} \rangle, \qquad (1)$$

where M is the atomic mass, $\mathbf{q}$ and $\mathbf{k}$ are wave vectors, and ij and ν denote indices of energy bands and phonon modes, respectively. $\omega_{\mathbf{q}\nu}$ and $\hat{e}_{\mathbf{q}\nu}$ stand for the phonon frequency and eigenvector of the νth phonon mode with wave vector $\mathbf{q}$. $dV_{\mathrm{SCF}}/d\hat{u}_{\mathbf{q}\nu}$ measures the change of self-consistent potential induced by atomic displacement. $\psi_{i,\mathbf{k}}$ and $\psi_{j,\mathbf{k}+\mathbf{q}}$ are Kohn-Sham orbitals.

The phonon linewidth $\gamma_{\mathbf{q}\nu}$ is defined by the integration [30,31],

$$\gamma_{\mathbf{q}\nu} = \frac{2\pi\omega_{\mathbf{q}\nu}}{\Omega_{\mathrm{BZ}}} \sum_{ij} \int d^3k \left| g^{ij}_{\mathbf{k},\mathbf{q}\nu} \right|^2 \delta(\epsilon_{\mathbf{q},i} - \epsilon_F)\delta(\epsilon_{\mathbf{k}+\mathbf{q},j} - \epsilon_F), \qquad (2)$$

where $\epsilon_{\mathbf{q},i}$ and $\epsilon_{\mathbf{k}+\mathbf{q},j}$ are eigenvalues of Kohn-Sham orbitals at given bands and wave vectors. The spectral function can be expressed as [30,31]

$$\alpha^2F(\omega) = \frac{1}{2\pi N(\epsilon_F)} \sum_{\mathbf{q}\nu} \delta(\omega - \omega_{\mathbf{q}\nu}) \frac{\gamma_{\mathbf{q}\nu}}{\hbar\omega_{\mathbf{q}\nu}}, \qquad (3)$$

where $N(\epsilon_F)$ is the density of states at the Fermi level. The EPC constant λ can be determined through summation over the first Brillouin zone or integration of the spectral function in frequency space [30,31],

$$\lambda = \sum_{\mathbf{q}\nu} \lambda_{\mathbf{q}\nu} = 2\int \frac{\alpha^2F(\omega)}{\omega} d\omega, \qquad (4)$$

where the EPC constant $\lambda_{\mathbf{q}\nu}$ for mode ν at wave vector $\mathbf{q}$ is defined by [30,31]

$$\lambda_{\mathbf{q}\nu} = \frac{\gamma_{\mathbf{q}\nu}}{\pi\hbar N(e_F)\omega^2_{\mathbf{q}\nu}}. \qquad (5)$$

Finally, the superconducting transition temperature T_c is determined by the Allen-Dynes formula [30,31],

$$T_c = \frac{\omega_{\log}}{1.2} \exp\left[\frac{-1.04(1+\lambda)}{\lambda(1-0.62\mu^*)-\mu^*}\right], \qquad (6)$$

where μ^* is the effective screened Coulomb repulsion constant whose value is generally between 0.1 and 0.15 [32,33], and $\omega_{\log}$ is the logarithmic average frequency

$$\omega_{\log} = \exp\left[\frac{2}{\lambda}\int \frac{d\omega}{\omega}\alpha^2F(\omega)\log\omega\right]. \qquad (7)$$

We further use a recently developed Wannier interpolation technique to reevaluate the EPC of $\mathrm{Li_3B_4C_2}$. In the Wannier interpolation calculation, we first use the local density approximation (LDA), combining with the norm-conserving pseudopotentials [34,35] to calculate the Bloch states and the phonon perturbation potentials [36]. The kinetic energy cutoff and the charge density cutoff of the plane wave basis are chosen to be 60 Ry and 240 Ry, respectively. The charge density of $\mathrm{Li_3B_4C_2}$ is calculated on a Γ-centered Brillouin-zone mesh of $16 \times 16 \times 24$ points, and a Methfessel-Paxton smearing [37] of 0.02 Ry. The phonons are calculated on a Γ-centered $4 \times 4 \times 6$ mesh, within the framework of density-functional perturbation theory [28]. Maximally localized Wannier functions [38,39] are constructed on a $4 \times 4 \times 6$ grid of the Brillouin zone, using the p_z and hybridized σ-like orbitals of boron and carbon atoms. Fine electron ($40 \times 40 \times 60$) and phonon ($20 \times 20 \times 30$) grids are used to interpolate the EPC constant with the Wannier90 and EPW codes [40,41]. Dirac δ functions for electrons and phonons are replaced by smearing functions with widths of 100 and 0.5 meV, respectively. The fully relaxed lattice constants along the a and c axes, i.e., 4.8492 Å and 3.5475 Å for $\mathrm{Li_3B_4C_2}$, are used in the Wannier interpolation calculation.

III. RESULTS AND ANALYSIS

$\mathrm{Li_3B_4C_2}$ is a layered compound which is formed by substituting one-third carbon with boron atoms from the semiconducting compound LiBC, with the remaining carbon atoms forming a regular hexagonal lattice in each boron-carbon layer. Figure 1 shows the crystal structure of this compound. From the first-principles density functional calculations, we find that the lattice constants of $\mathrm{Li_3B_4C_2}$ after full relaxation are 4.8669 Å and 3.5092 Å along the a and c axes, respectively. The bond lengths of boron-carbon and boron-boron bonds

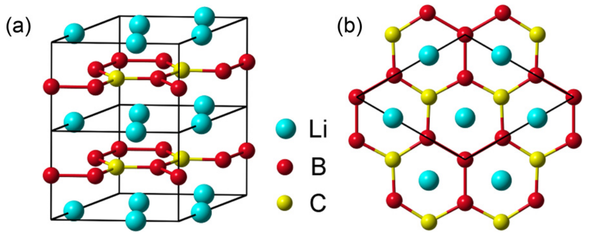

FIG. 1. (Color online) Crystal structure of $\mathrm{Li_3B_4C_2}$. (a) Three-dimensional view (two unit cells). (b) Top view. The cyan, red, and yellow balls represent lithium, boron, and carbon, respectively. The thick black line denotes the unit cell.

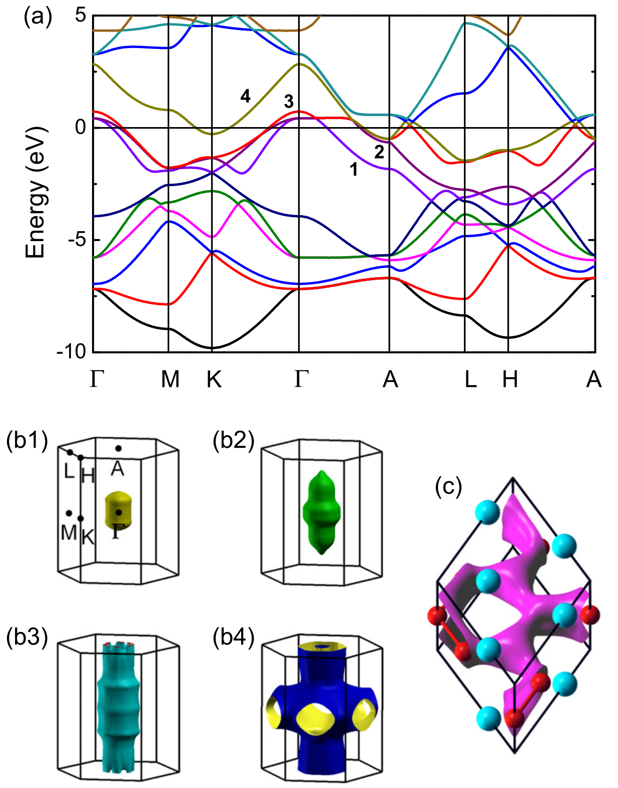

FIG. 2. (Color online) Electronic structure of $Li_3B_4C_2$. (a) Band structure. The Fermi level is set to zero. (b1)–(b4) Fermi surfaces corresponding to the four bands labeled in (a). (b1) also contains the high-symmetry points in the Brillouin zone in fractional coordinates, M ($\frac{1}{2}$,0,0), K ($\frac{1}{3}$,$\frac{1}{3}$,0), A (0,0,$\frac{1}{2}$), L ($\frac{1}{2}$,0,$\frac{1}{2}$), and H ($\frac{1}{3}$,$\frac{1}{3}$,$\frac{1}{2}$). (c) Isosurface of integrated local density of states from the Fermi level up to 750 meV (isovalue: 3.5 e/bohr^3 × 10^{-3}).

are 1.5902 Å and 1.6887 Å, respectively. Using subscripts b and c to represent boron and carbon atoms, we find that the bond angles are $\theta_{bcb} = \theta_{bbb} = 120^\circ$, $\theta_{cbc} = 124.14^\circ$, and $\theta_{cbb} = 117.93^\circ$.

Figure 2 shows the electronic band structure, Fermi surface, and spatial distribution of integrated local density of states for $Li_3B_4C_2$. There are four energy bands crossing the Fermi level. They form four Fermi surfaces: a small hole pocket [Fig. 2(b1)] and a spindle-shaped hole Fermi surface [Fig. 2(b2)] around Γ, a hole cylinder along the Γ-A direction [Fig. 2(b3)], and a multiterminal tubelike electron Fermi surface [Fig. 2(b4)]. The integrated local density of states [Fig. 2(c)] from the Fermi level up to 750 meV is distributed mainly around boron and carbon atoms. This suggests that there are two-dimensional sp^2-hybridized σ-bonding bands crossing the Fermi level.

To quantify the electron-phonon interaction, we calculate the phonon spectra and the EPC matrix elements for $Li_3B_4C_2$. Figure 3(a) shows the phonon spectrum. From our calculations, we find that there is no imaginary frequency along the high-symmetry lines in the Brillouin zone. It suggests that $Li_3B_4C_2$ is dynamically stable [42]. Similar to the E_{2g} mode in MgB_2, the twofold degenerate E' phonon modes around 73 meV have a large contribution to the electron-phonon interaction along the Γ-A line. The E' mode is a two dimensional bond-stretching optical mode. Its vibrational configuration is shown schematically in Figs. 3(b) and 3(c). Figure 3(d) shows how the band structure is changed before and after adding a perturbation to deform the lattice structure with an atomic displacement of 0.1 Å associated with the E' phonon mode. The projected weights of hybridized-sp^2 orbitals and p_z orbitals are also shown in Fig. 3(d), represented by red and blue colors, respectively. Among the four energy bands crossing the Fermi level, two of them are σ-bonding bands and the others are π-bonding bands. The orbital-resolved calculation further shows that each sp^2 orbital contributes almost equally to the σ-bonding states. The E' phonon mode breaks the degeneracy and splits the σ bands by 1.22 eV along Γ-A line. This indicates that there is a strong coupling between the E' phonon modes and the σ-bonding electrons, consistent with the direct EPC calculation shown in Fig. 3(a).

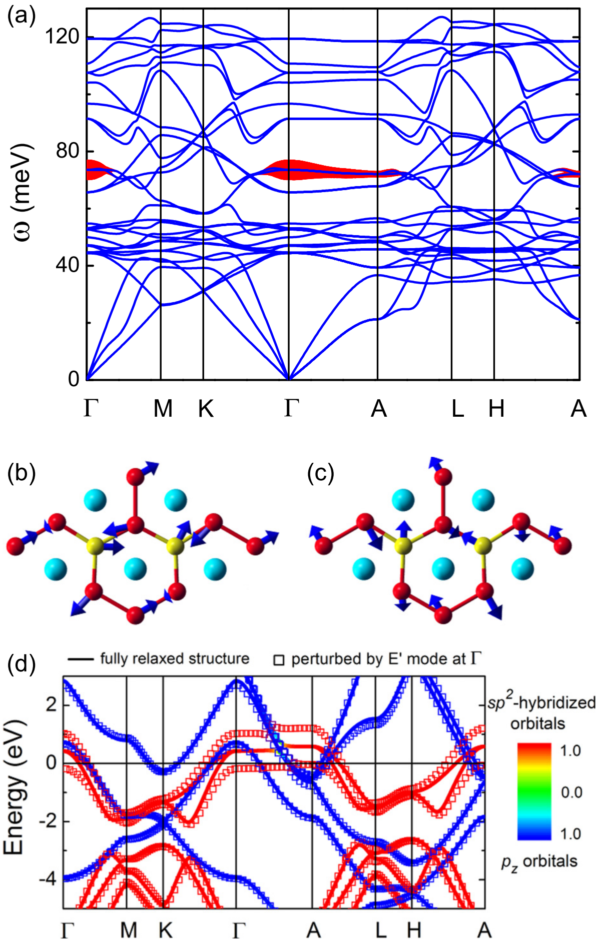

FIG. 3. (Color online) Lattice dynamics of $Li_3B_4C_2$. (a) Calculated phonon dispersion curves, in which the thickness of the red curve denotes the strength of the EPC at given wave vectors and modes. (b),(c) The twofold degenerate E' phonon modes along the Γ-A line near 73 meV having strong coupling with electrons. The blue arrows and their lengths represent the directions and relative amplitudes of these vibration modes, respectively. (d) Band structure with frozen-in E' mode (hollow square), compared with that of the fully relaxed structure (solid line). The contributions of the σ-bonding and π-bonding bands to the Kohn-Sham states at given **k** points and band indices are represented by red and blue colors, respectively.

From the above results, we calculated the phonon density of states, $F(\omega)$, and the Eliashberg spectral function, $\alpha^2 F(\omega)$,

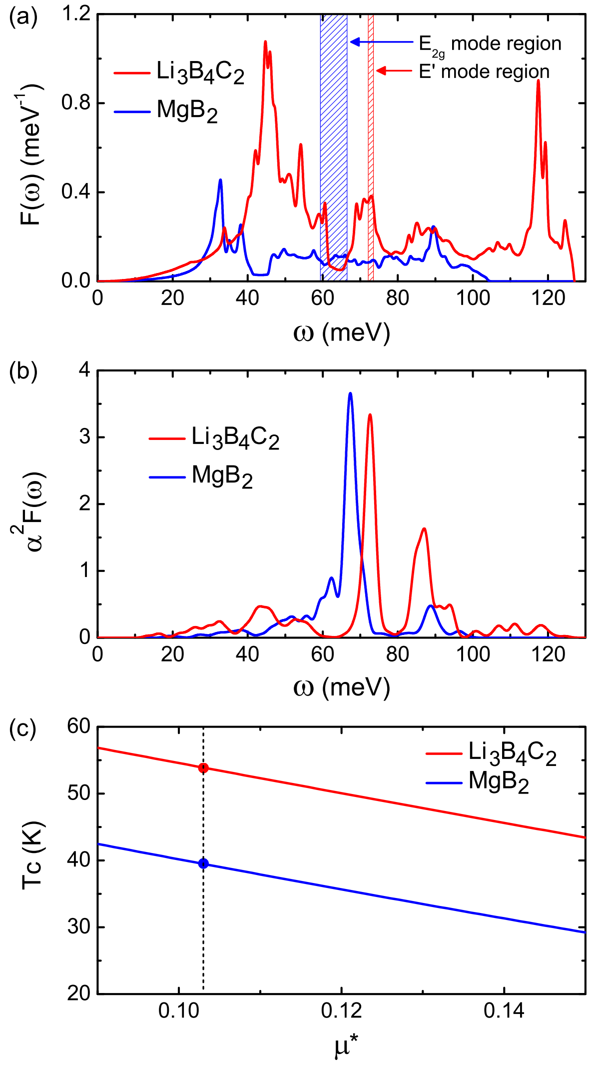

FIG. 4. (Color online) (a) Comparison of the density of states $F(\omega)$ of $Li_3B_4C_2$ with that of MgB_2. The regions of frequency for the E' mode in $Li_3B_4C_2$ and the E_{2g} mode in MgB_2 along the Γ-A direction are labeled by red and blue shadows, respectively. (b) Eliashberg spectral function $\alpha^2F(\omega)$ for $Li_3B_4C_2$ and MgB_2. (c) Evaluated T_c as a function of μ^* for $Li_3B_4C_2$ and MgB_2, respectively.

for $Li_3B_4C_2$. The results are shown in Figs. 4(a) and 4(b) and compared with MgB_2. Our results for the phonon density of state and the Eliashberg spectral function for MgB_2 agree well with those published by other groups [3,43], which were used to describe the specific heat [44], tunneling [45], penetration depth [46], and other experimental data [47]. In MgB_2, the Eliashberg spectral function is predominantly determined by the coupling between the σ-bonding band electrons and the bond-stretching E_{2g} mode. This leads to a dominant single-peak structure in $\alpha^2F(\omega)$ [Fig. 4(b)]. For the phonon density of states of $Li_3B_4C_2$ [Fig. 4(a)], besides two main peaks around 45 meV and 117 meV, there are two small peaks on the two sides of 80 meV [see red shading in Fig. 4(a)]. In comparison with the single-peak behavior of $\alpha^2F(\omega)$ in MgB_2, $\alpha^2F(\omega)$ of $Li_3B_4C_2$ shows two main peaks, resulting from the two-peak structure of $F(\omega)$ around 80 meV.

Knowing the Eliashberg spectral function, one can calculate the EPC constant λ, the logarithmic average frequency $\omega_{\log}$, and then the superconducting transition temperature T_c using the Allen-Dynes equation [31]. For MgB_2, we find that $\lambda = 0.885$, in agreement with published data [3,4], but slightly larger than the results obtained with the Wannier interpolation technique [48–50]. The logarithmic average frequency $\omega_{\log}$ is 60.82 meV, consistent with the results previously published [2,3,5,6,43,49]. The value of the effective screened Coulomb potential μ^* in the Allen-Dynes equation cannot be determined by the first-principles calculations. Empirically, μ^* takes a value between 0.10 and 0.15 [32,33]. By taking $\mu^* = 0.103$, we find that the superconducting transition temperature is 39.5 K for MgB_2, in agreement with the experimental observation.

For $Li_3B_4C_2$, we find that the EPC constant λ is equal to 1.114, which is about 25% larger than that of MgB_2, due to the two-peak structure in $F(\omega)$ around the energy of the E' phonon mode in $Li_3B_4C_2$. The value $\omega_{\log}$ is found to be 57.74 meV for $Li_3B_4C_2$, which is slightly lower than the corresponding value for MgB_2. Using the same μ^*, we find that the superconducting transition temperature of $Li_3B_4C_2$ is about 53.8 K, higher than the critical temperature of MgB_2. It is also higher than the superconducting transition temperature of $LiB_{1.1}C_{0.9}$ predicted by Miao *et al.* using the virtual crystal approximation (36 K) [51]. Figure 4(c) shows the superconducting transition temperature T_c as a function of μ^*. T_c drops almost linearly with μ^* for both materials in the range from 0.10 to 0.15. But for $Li_3B_4C_2$ the transition temperature T_c is still above 40 K even for $\mu^* = 0.15$.

In order to reduce the finite-size effect in the Brillouin zone sampling, we have also calculated the lattice dynamics and the EPC using the recently developed Wannier interpolation technique [36,41] for $Li_3B_4C_2$. Figure 5 shows the Eliashberg spectral function $\alpha^2F(\omega)$ of $Li_3B_4C_2$ calculated using the Wannier interpolation. In comparison with the results of $\alpha^2F(\omega)$ obtained by the direct calculation in the Bloch representation, the main peak is slightly red-shifted. The sharp peaks of $\alpha^2F(\omega)$ obtained directly in the Bloch representation are replaced by some fine structures. The EPC constant and $\omega_{\log}$ computed by integration in frequency space are 1.448 and 42.13 meV, respectively. Utilizing the Allen-Dynes formula and taking $\mu^* = 0.1$, the superconducting temperature T_c for $Li_3B_4C_2$ is found to be 53.9 K, in good agreement with the

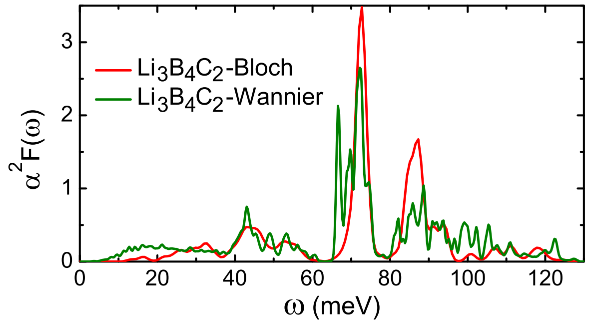

FIG. 5. (Color online) Comparison of the Eliashberg spectral functions $\alpha^2F(\omega)$ for $Li_3B_4C_2$ obtained by the direct calculation in the Bloch representation and the Wannier interpolation technique.

result directly calculated in the Bloch representation. Thus both methods, namely the direct calculation in the Bloch representation and that with the Wannier interpolation, confirm that $Li_3B_4C_2$ is a strong phonon-mediated superconductor whose T_c is higher than that of MgB_2.

IV. DISCUSSION AND SUMMARY

The strong EPC in $Li_3B_4C_2$ may raise the question of associated lattice instabilities. To examine the stability of this compound, we calculate the static formation energy and find that it is 0.631 eV/Li lower than the energy for the corresponding constituent elemental solids (i.e., body-centered cubic lithium, graphite, and α-B_{12}). This, together with the absence of imaginary phonon frequency, shows that this compound is dynamically stable. It suggests that this material can be synthesized in the laboratory from the constituent elemental solids. Considering the fact that high-quality single crystals of LiBC are available, we believe that it is highly feasible to grow high quality $Li_3B_4C_2$ films on a LiBC substrate by molecular beam epitaxy (MBE). The tensile stress between the film and the substrate can stabilize the crystal structure of $Li_3B_4C_2$ even if it has a lattice instability.

In summary, we propose that there is high possibility to find a strong electron-phonon coupled high-temperature superconductor if one can lift σ bonding or other strong chemical bonding band up to the Fermi level. Based on this picture and first-principles calculations, we predict that stoichiometric $Li_3B_4C_2$ is a phonon-mediated high-T_c superconductor with a T_c above 50 K. The strong electron-phonon coupling in this material results from the interaction between the σ-bonding band electrons and the bond-stretching E' phonons.

ACKNOWLEDGMENTS

We thank Professor Bruce Normand for his critical reading of the manuscript. This work is supported by the National Natural Science Foundation of China (Grant No. 11190024) and the National Program for Basic Research of MOST of China (Grant No. 2011CBA00112).

APPENDIX A: ELECTRON-PHONON COUPLING OF Li_2B_3C

Li_2B_3C is a layered material, which is obtained by substituting half of the boron-carbon layers by pure boron layers from compound LiBC. The crystal structure of Li_2B_3C is shown in Fig. 6. From the first-principles calculations, we find that Li_2B_3C is inherently a metal with two σ-bonding bands crossing the Fermi level. As expected, the coupling of these σ-bonding bands with optical phonons is very strong, which can drive this material into a high-T_c superconducting state.

The lattice parameters we obtained from the first-principles calculations for LiBC along a and c axes are 2.7355 Å and 7.0173 Å, respectively, which agree accurately with the experimental data [17]. Since the radius of the boron atom is larger than that of carbon, the lattice parameters of Li_2B_3C are slightly enlarged in comparison with those of LiBC. The lattice parameters after full relaxation for Li_2B_3C are 2.8305 Å and 7.1082 Å along the a and c axes, respectively.

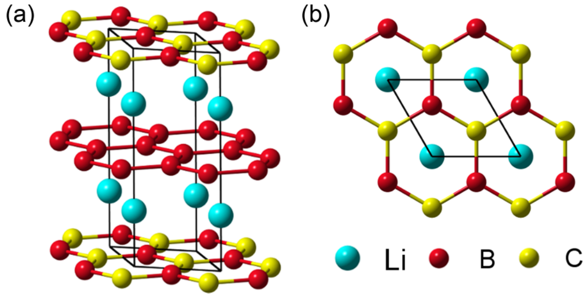

FIG. 6. (Color online) Crystal structure of Li_2B_3C, containing pure honeycomb boron layers. (a) Three-dimensional view. (b) Top view. The cyan, red, and yellow balls represent lithium, boron, and carbon, respectively. The black line denotes the unit cell.

Due to the absence of inversion symmetry between boron-carbon and boron-boron layers in Li_2B_3C, lithium atoms move slightly towards the honeycomb boron-boron layers.

Figure 7 shows the electronic band structure for Li_2B_3C. In both boron-carbon and pure boron layers, the hybridization of atomic orbitals generates two different kinds of bonds, one is the sp^2 hybridized σ bond, and the other is the p_z overlapped π bond. There are four σ-bonding bands around the Fermi level. These bands, represented by the blue and red lines in Fig. 7(a), are highly two-dimensional and characterized by the dispersionless energy-momentum curves along the k_z (i.e., Γ-A) direction. Two of them cross the Fermi level and each exhibits a cylindrical-like Fermi surface around the zone center [Fig. 7(c)]. These two bands are formed mainly by the σ electrons in the honeycomb boron layers. The other two σ-bonding bands, which are about 0.4 eV below the Fermi energy, are mainly contributed by σ electrons in the boron-carbon layers and confirmed by the result of partial density of states shown in Fig. 7(d). In comparison with the boron-carbon layer, the pure boron layer has one less electron in every unit cell and can be regarded as an intrinsically hole-doped subsystem. That is the reason why only the σ-bonding band from the pure boron layer can appear on the Fermi level.

Besides the two σ-bonding bands, there are also two π-bonding bands crossing the Fermi level. They show strong dispersion along the k_z direction. One of them shows a warped hole Fermi surface sheet around the zone boundary and a Dirac conelike band dispersion at H about 1 eV above the Fermi level. The other π-bonding band shows six hole pocketlike Fermi surface sheets at the zone corners [Fig. 7(c)]. Similar to the case of MgB_2, the energy overlap between σ-bonding and π-bonding bands at the Fermi level is caused by the attraction of cations [2,52]. The decrease in the density of states between 0.5 eV and 1.3 eV [Fig. 7(d)] originates in the linear dispersion of Dirac conelike bands. In comparison with the σ and π electrons, the contribution to the density of states near the Fermi level from Li-2s and Li-2p orbitals is negligibly small.

To quantify the EPC properties, we calculate the phonon spectra and the Eliashberg spectral function. Figure 8(a) shows the phonon dispersion curves along the high-symmetry lines in the Brillouin zone and the phonon density of states. In comparison with the E_{2g} mode in MgB_2, we find that there are basically four phonon modes, which account for the majority of the EPC in Li_2B_3C. They are the A_1' mode at Γ, the E'

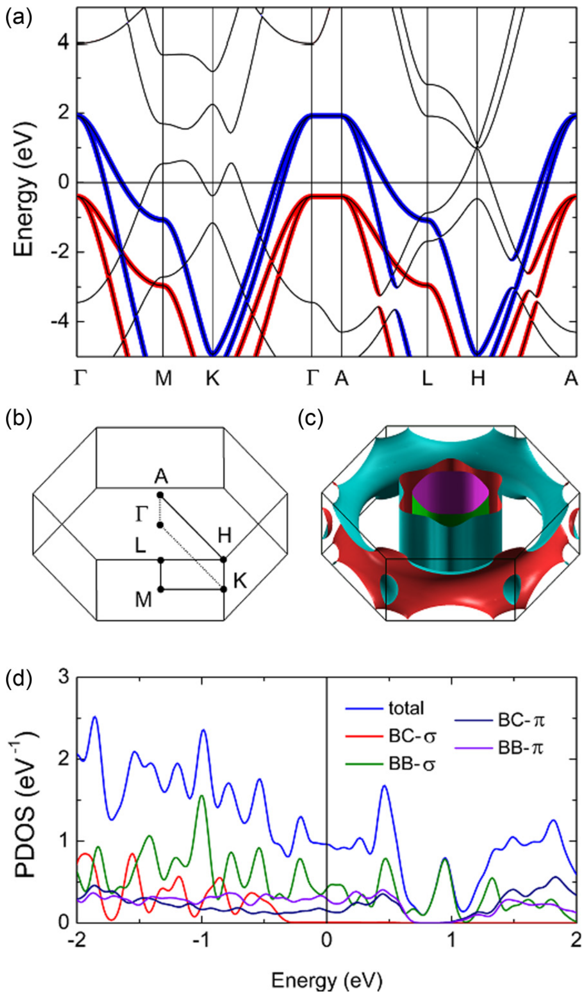

FIG. 7. (Color online) Electronic structures of Li_2B_3C. (a) Band structure, where the thicknesses of blue and red lines are proportional to the weights of the σ bonds from the boron-carbon and pure boron layers, respectively. (b) High-symmetry points in the Brillouin zone. (c) Fermi surfaces. (d) Orbital-resolved partial density of states (PDOS). BB and BC represent pure boron and boron-carbon layers, respectively.

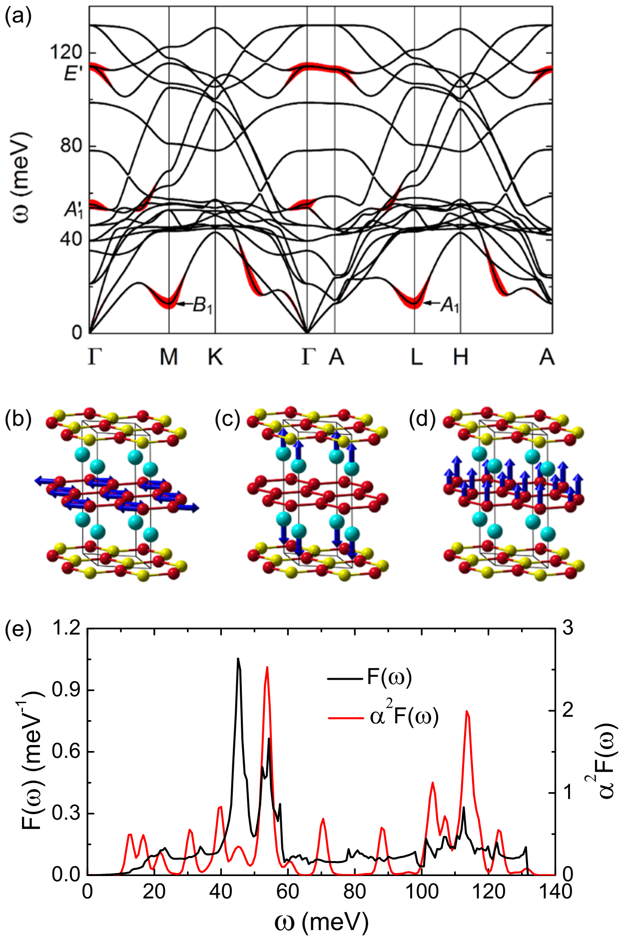

FIG. 8. (Color online) Calculated lattice dynamics and EPC for Li_2B_3C. (a) Phonon dispersion curves. The thicknesses of the red lines denote the strength of EPC constant for a given wave vector and mode $\lambda_{\mathbf{q}\nu}$. A_1', B_1, A_1, and E' are the phonon modes which have relatively large EPC at the high-symmetry points. Vibrational configurations for the twofold degenerate E' mode at Γ with $\omega \simeq 115$ meV (b), the A_1' mode at Γ with $\omega \simeq 55$ meV (c), the B_1 mode at M, or the A_1 mode at L with $\omega \simeq 15$ meV (d), respectively. The blue arrows represent the directions of vibrations, and their lengths denote the relative amplitudes. (e) Phonon density of states $F(\omega)$ and Eliashberg spectral function $\alpha^2F(\omega)$.

mode along the Γ-A line, the B_1 mode at M, and the A_1 mode at L. A graphical representation of these modes is shown in Figs. 8(b)–8(d). The E' mode is a twofold degenerate bond-stretching optical mode, with intralayer movements of boron atoms in the boron layer, which is analogous to the E_{2g} mode in MgB_2. The A_1' mode represents an opposite displacement between two Li layers towards the honeycomb boron-carbon layer. The B_1 and A_1 modes are two interlayer vibrations of boron atoms in the boron layer. The magnitudes of the EPC constants at the high-symmetry points for these phonon modes are shown in Fig. 8(a) by the thickness of the red curves.

From the above results, we calculate the Eliashberg spectral function $\alpha^2F(\omega)$ for Li_2B_3C. The multipeak behavior in $\alpha^2F(\omega)$ is a natural reflection of the existence of multiple phonon modes that couple strongly with electrons [Fig. 8(e)]. The two main peaks in $\alpha^2F(\omega)$ around 55 meV and 115 meV correspond to the couplings of electrons with the A_1' and E' phonon modes, respectively. The EPC constant λ is equal to 1.566, about 77% higher than the corresponding value for MgB_2. But the value of $\omega_{\log}$ is 40.26 meV, about 34% smaller than that of MgB_2. Taking $\mu^* = 0.103$ as in the main text, we find $T_c = 54.9$ K for Li_2B_3C.

APPENDIX B: FORMATION ENERGIES

The EPC constant λ in Li_2B_3C is larger than that of $Li_3B_4C_2$ presented in the main text, but the excess boron atoms are not uniformly distributed in boron-carbon layers in Li_2B_3C. Thus the tensile stress in Li_2B_3C is not well balanced, unlike in $Li_3B_4C_2$. In order to determine which compound is more stable, we calculate the formation energies for Li_2B_3C (abbreviated as E_{231}) and $Li_3B_4C_2$ (abbreviated as E_{342}).

Here the formation energy is defined as

$$E_{\text{tot}} - (E_{\text{Li}} + (1+x)E_{\text{B}} + (1-x)E_{\text{C}}), \qquad \text{(B1)}$$

where E_{Li}, E_{B}, and E_{C} are respectively the energy per atom for elemental solids of body-centered cubic lithium, graphite, and α-B_{12} [53]. E_{tot} is the total energy per lithium of $\mathrm{LiB}_{1+x}\mathrm{C}_{1-x}$, with x equal to $\frac{1}{2}$ and $\frac{1}{3}$ for $\mathrm{Li_2B_3C}$ and $\mathrm{Li_3B_4C_2}$, respectively. We find that the formation energy of $\mathrm{Li_2B_3C}$ is $E_{231} = -0.429$ eV/Li and the corresponding energy for $\mathrm{Li_3B_4C_2}$ is $E_{342} = -0.631$ eV/Li. This means that $\mathrm{Li_3B_4C_2}$ is energetically more stable than $\mathrm{Li_2B_3C}$.

The boron-carbon layers in $\mathrm{Li_3B_4C_2}$ presented in the main text take AA-stacking patterns along the z axis. We have also calculated the total energies of various AB-stacking configurations of boron-carbon layers for $\mathrm{Li_3B_4C_2}$. It is found that the energy difference between AA stacking and the most stable AB-stacking patterns is 0.002 eV/Li, which indicates that the influence of different stacking patterns on the electronic structures is negligible.

---

[1] J. Nagamatsu, N. Nakagawa, T. Muranaka, Y. Zenitani, and J. Akimitsu, Nature (London) **410**, 63 (2001).

[2] J. M. An and W. E. Pickett, Phys. Rev. Lett. **86**, 4366 (2001).

[3] Y. Kong, O. V. Dolgov, O. Jepsen, and O. K. Andersen, Phys. Rev. B **64**, 020501(R) (2001).

[4] T. Yildirim *et al.*, Phys. Rev. Lett. **87**, 037001 (2001).

[5] H. J. Choi, D. Roundy, H. Sun, M. L. Cohen, and S. G. Louie, Phys. Rev. B **66**, 020513(R) (2002).

[6] H. J. Choi, D. Roundy, H. Sun, M. L. Cohen, and S. G. Louie, Nature (London) **418**, 758 (2002).

[7] S. L. Bud'ko, G. Lapertot, C. Petrovic, C. E. Cunningham, N. Anderson, and P. C. Canfield, Phys. Rev. Lett. **86**, 1877 (2001).

[8] X. Blase, E. Bustarret, C. Chapelier, T. Klein, and C. Marcenat, Nat. Mater. **8**, 375 (2009).

[9] E. A. Ekimov *et al.*, Nature (London) **428**, 542 (2004).

[10] Y. Takano *et al.*, Diamond Relat. Mater. **16**, 911 (2007).

[11] J. E. Moussa and M. L. Cohen, Phys. Rev. B **77**, 064518 (2008).

[12] V. L. Solozhenko, O. O. Kurakevych, D. Andrault, Y. Le Godec, and M. Mezouar, Phys. Rev. Lett. **102**, 015506 (2009).

[13] T. E. Weller *et al.*, Nat. Phys. **1**, 39 (2005).

[14] A. Gauzzi *et al.*, arXiv:cond-mat/0603443.

[15] I. I. Mazin, Phys. Rev. Lett. **95**, 227001 (2005).

[16] J. S. Kim, L. Boeri, R. K. Kremer, and F. S. Razavi, Phys. Rev. B **74**, 214513 (2006).

[17] M. Wörle, R. Nesper, G. Mair, M. Schwarz, and H. G. Vonschnering, Z. Anorg. Allg. Chem. **621**, 1153 (1995).

[18] P. F. Karimov *et al.*, J. Phys.: Condens. Matter **16**, 5137 (2004).

[19] H. Rosner, A. Kitaigorodsky, and W. E. Pickett, Phys. Rev. Lett. **88**, 127001 (2002).

[20] A. Bharathi *et al.*, Solid State Commun. **124**, 423 (2002).

[21] D. Souptela, Z. Hossainb, G. Behra, W. Lösera, and C. Geibel, Solid State Commun. **125**, 17 (2003).

[22] A. M. Fogg, P. R. Chalker, J. B. Claridge, G. R. Darling, and M. J. Rosseinsky, Phys. Rev. B **67**, 245106 (2003).

[23] A. M. Fogg, J. Meldrum, G. R. Darling, J. B. Claridge, and M. J. Rosseinsky, J. Am. Chem. Soc. **128**, 10043 (2006).

[24] P. Giannozzi *et al.*, J. Phys.: Condens. Matter **21**, 395502 (2009).

[25] J. P. Perdew, K. Burke, and M. Ernzerhof, Phys. Rev. Lett. **77**, 3865 (1996).

[26] A. M. Rappe, K. M. Rabe, E. Kaxiras, and J. D. Joannopoulos, Phys. Rev. B **41**, 1227 (1990).

[27] N. Marzari, D. Vanderbilt, A. De Vita, and M. C. Payne, Phys. Rev. Lett. **82**, 3296 (1999).

[28] S. Baroni, S. de Gironcoli, A. Dal Corso, and P. Giannozzi, Rev. Mod. Phys. **73**, 515 (2001).

[29] G. M. Eliashberg, Zh. Eksp. Teor. Fiz. **38**, 966 (1960) [Sov. Phys. JETP (Engl. trans.) **11**, 696 (1960)].

[30] P. B. Allen, Phys. Rev. B **6**, 2577 (1972).

[31] P. B. Allen and R. C. Dynes, Phys. Rev. B **12**, 905 (1975).

[32] C. F. Richardson and N. W. Ashcroft, Phys. Rev. Lett. **78**, 118 (1997).

[33] K.-H. Lee, K. J. Chang, and M. L. Cohen, Phys. Rev. B **52**, 1425 (1995).

[34] N. Troullier and J. L. Martins, Phys. Rev. B **43**, 1993 (1991).

[35] M. Fuchs and M. Scheffler, Comput. Phys. Commun. **119**, 67 (1999).

[36] F. Giustino, M. L. Cohen, and S. G. Louie, Phys. Rev. B **76**, 165108 (2007).

[37] M. Methfessel and A. T. Paxton, Phys. Rev. B **40**, 3616 (1989).

[38] N. Marzari and D. Vanderbilt, Phys. Rev. B **56**, 12847 (1997).

[39] I. Souza, N. Marzari, and D. Vanderbilt, Phys. Rev. B **65**, 035109 (2001).

[40] A. A. Mostofi, J. R. Yates, Y.-S. Lee, I. Souza, D. Vanderbilt, and N. Marzari, Comput. Phys. Commun. **178**, 685 (2008).

[41] J. Noffsinger, F. Giustino, B. D. Malone, C.-H. Park, S. G. Louie, and M. L. Cohen, Comput. Phys. Commun. **181**, 2140 (2010).

[42] There are 27 independent vibration modes for $\mathrm{Li_3B_4C_2}$. A lattice instability occurs if the frequencies of one or a few of these 27 modes become imaginary. For $\mathrm{Li_3B_4C_2}$, we have sampled the phonon wave vectors on $N_q \times N_q \times N_q$ mesh, with N_q varying from 5 to 9, and do not find any imaginary frequency at these sampled wave vectors and in the Fourier interpolated phonon spectrum along the high-symmetry lines. This suggests that $\mathrm{Li_3B_4C_2}$ is dynamically stable.

[43] K.-P. Bohnen, R. Heid, and B. Renker, Phys. Rev. Lett. **86**, 5771 (2001).

[44] A. A. Golubov *et al.*, J. Phys: Condens. Matter **14**, 1353 (2002).

[45] A. Brinkman, A. A. Golubov, H. Rogalla, O. V. Dolgov, J. Kortus, Y. Kong, O. Jepsen, and O. K. Andersen, Phys. Rev. B **65**, 180517 (2002).

[46] A. A. Golubov, A. Brinkman, O. V. Dolgov, J. Kortus, and O. Jepsen, Phys. Rev. B **66**, 054524 (2002).

[47] O. V. Dolgov, R. K. Kremer, J. Kortus, A. A. Golubov, and S. V. Shulga, Phys. Rev. B **72**, 024504 (2005).

[48] A. Eiguren and C. Ambrosch-Draxl, Phys. Rev. B **78**, 045124 (2008).

[49] M. Calandra, G. Profeta, and F. Mauri, Phys. Rev. B **82**, 165111 (2010).

[50] E. R. Margine and F. Giustino, Phys. Rev. B **87**, 024505 (2013).

[51] R. Miao *et al.*, J. Appl. Phys. **113**, 133910 (2013).

[52] J. Kortus, I. I. Mazin, K. D. Belashchenko, V. P. Antropov, and L. L. Boyer, Phys. Rev. Lett. **86**, 4656 (2001).

[53] B. F. Decker and J. S. Kasper, Acta Crystallogr. **12**, 503 (1959).